ACS Photonics

Article

Cite This: ACS Photonics 2019, 6, 2260−2267

pubs.acs.org/journal/apchd5

Nanostructured Radiation Emitters: Design Rules for High-Performance Thermophotovoltaic Systems

Younghoe Kim,[†] Mun-Jong Kim,[†] Young-Seok Kim,[‡] Hyunjung Lee,*[,†] and Sung-Min Lee*[,†]

[†]School of Materials Science and Engineering, Kookmin University, 77 Jeongneung-ro, Seongbuk-gu, Seoul 02707, Republic of Korea

[‡]Display Materials and Components Research Center, Korea Electronics Technology Institute, 25 Saenari-ro, Bundang-gu, Seongnam-si, Gyeonggi-do 13509, Republic of Korea

Supporting Information

ABSTRACT: Wavelength-selective, nanostructured metallic radiation emitters are investigated for high-performance thermophotovoltaic (TPV) systems. After building evaluation tools to find the highly efficient selective emitters, studies of achieve emitter design schemes are systematically conducted by employing characterization factors of spectral cutoff efficiency and effective emittance efficiency. With identified ideal emissivity spectra and optimum geometric parameters of the selective emitters through the proposed design scheme, simply fabricated, three-dimensional photonic emitters comprising nickel inverse opal (Ni IO) structures are experimentally demonstrated. The Ni IO emitters exhibit the enhanced performance in terms of both spectral cutoff efficiency and effective emittance efficiency, as their plasmonic resonance at designated wavelengths augments the absorption property and hence the radiation property. An issue of the thermal deterioration of Ni IO emitters at high temperatures is resolved by applying a passivation layer consisting of thermally stable ceramic material. Details of optimal design rule, fabrication procedure, and quantitative characterizations in conjunction with various case studies offer directions toward high-performance radiation emitters in the context of energy harvesting TPV systems.

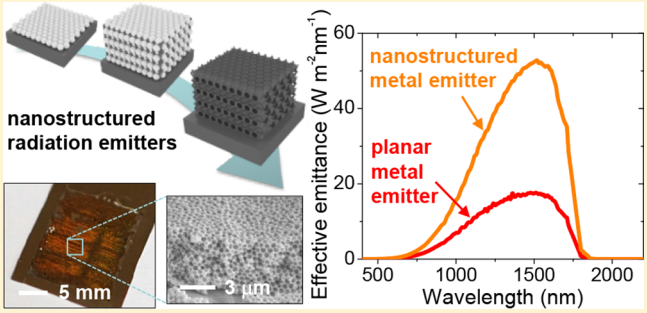

KEYWORDS: *selective radiation emitters, thermophotovoltaics, inverse opal nanostructures, metallic photonic crystals*

While thermophotovoltaic (TPV) systems consisting of radiation emitters and photovoltaic (PV) cells had been well established for several decades,[1,2] it had received less attention compared to the other classes of energy systems due to the inferior energy conversion efficiency.[3,4] Such unfriendly situation around TPV technologies has been fortunately changed after finding exceptionally effective emitters that allow the radiation only at selective wavelengths.[5−7] These wavelength-selective emitters can suppress the unabsorbable radiation with energy below a bandgap of PV cells, and hence significantly mitigate the energy loss. The selective emitters are especially vital when combined with full-spectrum solar absorbers, as they, so-called solar TPVs, provide a possibility to achieve the ideal limit of PV efficiency under the solar illumination.[3,8−10] Although introduction of the photonic filters that reflect the sub-bandgap photons before reaching the PV cells is another promising route to enhancing the efficiency of TPVs by retrieving unabsorbed radiation energy,[4,11−13] application of the selective emitters that can directly reduce the radiation energy loss is a still valuable option because it is consistently effective even when other classes of energy loss (e.g., conduction, convection, etc.) exist. The spectral selectivity function of emitters has been attained by doping metallic impurities into bulk ceramic materials,[14] rare-earth oxides,[15,16] or by forming one- or multidimensional photonic structures with metals.[7,17−19] Among the reported methods for obtaining the spectral selectivity, the photonic metal structures are particularly impressive due to the possibility to possess the near-completely stifled reflection in the long-wavelength range (>∼2 μm).[18,20,21] So far, many successful demonstrations of photonic-structured selective emitters have been made by using barely melted metals such as tungsten and tantalum with the structural stability at high temperatures,[5,6,9] where the selective emitters were designed to maximize the filtering property at the PV band-edge as the spectral filtering performance is indubitably a primary requirement of high-performance emitters. However, the TPV efficiency cannot be fully maximized through emitter design processes without consideration of various system factors (e.g., quantum efficiency of PV cells, nonradiation energy loss, etc.), because the energy delivery yield from emitters to PV cells is also affected by such system factors. In this regard, here we present an advanced scheme of emitter

Received: April 12, 2019
Published: August 14, 2019

DOI: 10.1021/acsphotonics.9b00560
ACS Photonics 2019, 6, 2260−2267

designs and experimental selective emitters consisting of three-dimensional metallic inverse opal (IO) structures that are tailored through this design scheme. The advanced design scheme employs novel characterization factors (e.g., spectral cutoff efficiency, effective emittance efficiency) that can contemplate the PV cell characteristics and TPV system environments. Considering that IO structures can allow the emissivity control without the direction dependency, as well as the design control through the facile manipulation of an opal template,[6,22] the metallic nickel (Ni) IO emitters fabricated via simple process methods[22−25] (e.g., self-assembly of polymer nanoparticles for an opal template, electrodeposition of Ni metal) are employed for the experimental demonstration. The thermal stability of Ni IO structures at a high temperature (∼1100 °C) is ensured with a thermally stable passivation layer of magnesium oxide (MgO) that can provide a solid anchoring property from its high melting point (∼2850 °C) and simultaneously alleviate Ni IO oxidation caused by the oxygen anion migration due to a low electron affinity value (−0.4 eV)[26] of Mg. Together with case studies of the advanced design scheme to identify ideally optimal emittance spectra of emitters, details of fabrication procedure and systematic characterizations based on both numerical simulations and experiments are provided to offer insights into pathways to achieve the high-performance TPV systems.

RESULTS AND DISCUSSION

Figure 1a schematically describes fabrication steps for the proposed Ni IO selective emitters with enhanced thermal stability. As a first step, a hexagonally close-packed monolayer of synthesized polystyrene (PS) particles was arranged on a polished Ni plate via the Langmuir−Blodgett method,[27] where PS particles with various diameters (250−1250 nm) were tested (Figure S1). This PS monolayer served as a seed layer to facilitate close packing of overall PS multilayers that were subsequently deposited by the slide-coating method (Figure S2),[28,29] thereby leading to a solid crystalline structure of a face-centered cubic (fcc) opal. A total thickness of the resultant PS opal structure was 15−20 μm at our experimental condition of using a solution of PS particles dispersed in water with a mixture ratio of 4 wt %. After formation of the PS opal template, its empty space was gradually occupied by Ni starting from the plate through the electrodeposition process, in which Ni, platinum (Pt), silver (Ag)/silver chloride (AgCl), and nickel(II)-sulfamate tetrahydrate ($Ni(SO_3NH_2)_2$)/boric acid (H_3BO_3) were used as working, counter, reference electrodes and electrolyte, respectively. The number of layers filled with the electrodeposited Ni was chosen as 15 by counting the number of oscillation in the current−time plot observed at the potentiostat (Figure S3).[30] By removing PS particles of the opal template with toluene, the complete Ni inverse opal (IO) structure was revealed. The thermal stability of Ni IO was enhanced by the following deposition of a ∼30 nm thick MgO passivation layer on its entire surfaces via the thermal atomic layer deposition (ALD) system with bis-(ethylcyclopentadienyl)magnesium ($Mg(CpEt)_2$) and water canisters.[31] Figure 1b, c, and d show the scanning electron microscope (SEM) images and photographs (insets) of samples at the representative process steps for formations of PS opal, Ni IO, and MgO-coated Ni IO structures, respectively, for a case of using PS nanoparticles with a diameter of ∼500 nm (i.e., a pattern period of ∼500 nm). The finely ordered Ni IO structure and its particular reflection color

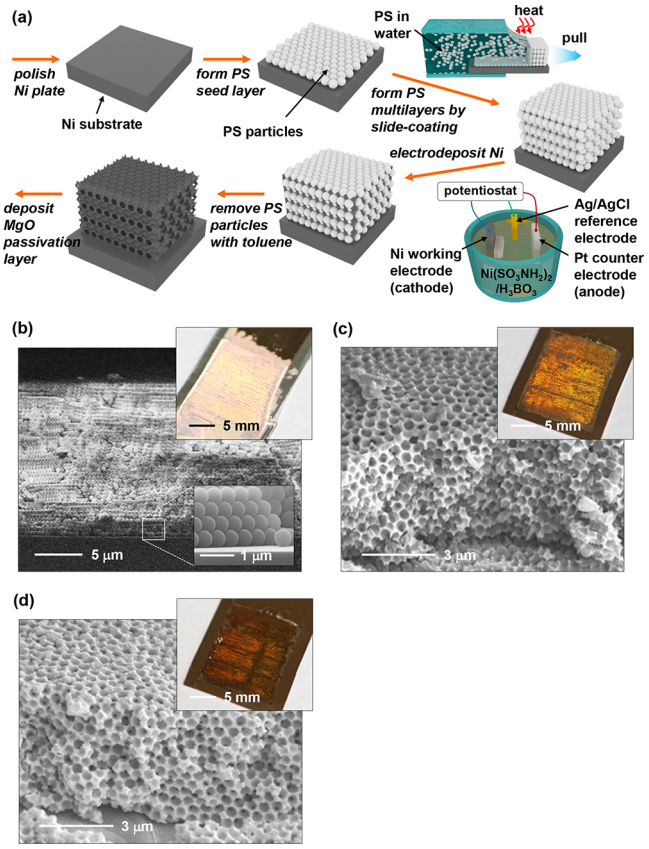

Figure 1. (a) Schematic illustration of the fabrication steps for the MgO-passivated Ni IO emitters. (b) Cross-sectional SEM image of the opal template comprising PS particles with a diameter of 500 nm. Upper and lower insets indicate photographic and magnified images of the corresponding sample. (c) Tiled-view SEM and photographic (inset) images of the Ni IO emitter created from the PS opal template of (b). Corresponding images of the Ni IO emitter after implementing the 30 nm thick MgO passivation.

can be observed in Figure 1c as a consequence of a delicately prepared PS opal template of Figure 1b. By virtue of the ALD method, it can be identified that the MgO passivation layer conformally covers both inner and outer surfaces of the Ni IO structure as shown in Figure 1d, where monitored reflection color of the MgO-coated Ni IO is red-shifted from that of the bare Ni IO due to the abated photonic resonance energy provoked by the raised effective refractive index of surrounding media. More detailed photographic images for samples with various pattern periods (e.g., 250, 500, 750, and 1250 nm) can be found in the Supporting Information (Figure S4).

Before designing selective radiation emitters for highly efficient TPVs, quantitative physical values that could evaluate the emitter performance were established to compare various emissivity spectra of emitters, and hence to identify an optimal emissivity spectrum. Given that the TPV efficiency was affected by not only the cutoff behavior of radiation spectra but also an absorptivity degree of PV cells with respect to the radiated energy from emitters, two characteristic yield factors of emitters, spectral cutoff efficiency (η_s) and effective emittance efficiency (η_e), were defined as follows:

$$\eta_s(T) = \frac{\int_{\lambda_0}^{\infty} \mathrm{EQE}_{\mathrm{PV}}(T, \lambda) M_e(T, \lambda) \mathrm{d}\lambda}{\int_{\lambda_0}^{\infty} M_e(T, \lambda) \mathrm{d}\lambda} \quad (1)$$

DOI: 10.1021/acsphotonics.9b00560
ACS Photonics 2019, 6, 2260−2267

$$\eta_e(T) = \frac{\int_{\lambda_0}^{\infty} \mathrm{EQE}_{PV}(T, \lambda) M_e(T, \lambda) d\lambda}{\int_{\lambda_0}^{\infty} \mathrm{EQE}_{PV}(T, \lambda) M_{e,BB}(T, \lambda) d\lambda} \quad (2)$$

where EQE_{PV}, T, and λ are external quantum efficiency of PV cells, temperature of emitter, and wavelength, respectively. M_e and $M_{e,BB}$ are spectral emittances of radiation emitter and ideal blackbody, respectively, in which M_e is calculated as the product of emissivity (ε_e) of emitter and $M_{e,BB}$ through an equation given by $M_e(\lambda) = \varepsilon_e(\lambda) M_{e,BB}(\lambda)$. The spectral cutoff efficiency (η_s) directly indicates effectiveness of the emitter radiation in generating the electric energy, because the quantitative amount of convertible radiation energy at PV cells is associated with a spectral function of the $\mathrm{EQE}_{PV}(\lambda)$. When a product of $\mathrm{EQE}_{PV}(\lambda)$ and $M_e(\lambda)$ is set to the spectral effective emittance ($M_{e,eff}(\lambda) = \mathrm{EQE}_{PV}(\lambda)\ M_e(\lambda)$), the η_s can be simply calculated as an integral of the spectral effective emittance divided by an integral of the spectral emittance. The η_s proposed herein conceptually corresponds to the filtering performance of radiation spectrum against the PV band-edge, which was frequently considered in the previous studies.[5,7,9] In fact, when employing an ideal PV absorber that can absorb all photons at wavelengths below a bandgap wavelength (λ_{bg}) and then convert them into the photocurrent without internal loss (i.e., $\mathrm{EQE}_{PV}(\lambda) = 1$ at $\lambda < \lambda_{bg}$, $\mathrm{EQE}_{PV}(\lambda) = 0$ at $\lambda > \lambda_{bg}$), the proposed η_s is obviously identical to the former characterization of the filtering performance. Nevertheless, practical PV absorber cells are nonideal, indicating that the present definition is more general. In the meantime, the emitter performance can be solely evaluated with a level of the η_s if the emitters are completely isolated as in vacuum (i.e., no conduction and convection), because there is no route of transferring the thermal energy, except the radiation. However, the typical emitters are not isolated, and therefore, another class of a characteristic factor of the emitter performance is required to assess the ability of mitigating the thermal energy loss in the system. Considering that a decay rate of the thermal energy of emitter through the conduction and convection processes can be a certain value dictated by a system configuration as well as a temperature level, the emitters with the higher radiation intensity at a given temperature are deemed more efficient due to enhanced dominance of the radiation decay. In order words, when the productive (i.e., absorbable) and unproductive (i.e., unabsorbable) radiation decay rates and nonradiation (i.e., conduction or convection) decay rate at a temperature T are denoted as $k_{pr}(T)$, $k_{upr}(T)$, and $k_{n-r}(T)$, respectively, the productive radiation efficiency ($\eta_{pr}(T)$) can be characterized with an equation given by $\eta_{pr}(T) = k_{pr}(T)/(k_{pr}(T) + k_{upr}(T) + k_{n-r}(T))$, where $\eta_{pr}(T)$ can be improved by the controlled emitter property with an increased $k_{pr}(T)$ value because the $k_{n-r}(T)$ is determined by the TPV device structure rather than the emitter property. From this point of view, the effective emittance efficiency (η_e) that was defined as a ratio of the amount of the convertible radiation power of emitter against that of the ideal blackbody (i.e., an integral of the effective emittance of an emitter normalized by an integral of the effective emittance of the blackbody) can be one possible option for this characteristic factor as it is directly proportional to the k_{pr}. A level of η_e becomes critical, especially for devices suffering from the large conduction or convection loss.

To find an ideal configuration of emissivity spectrum, representative emissivity spectra of emitters were examined with the proposed characteristic factors. The tested four emissivity spectra (ε_{e1}, ε_{e2}, ε_{e3}, and ε_{e4}) were specified by combination of unit step function ($u(\lambda)$; $u(\lambda) = 0$ for $\lambda < 0$, $u(\lambda) = 1$ for $\lambda > 0$) and ramp function ($R(\lambda)$; $R(\lambda) = 0$ for $\lambda < 0$, $R(\lambda) = \lambda$ for $\lambda > 0$), given by

$$\text{case 1:}\quad \varepsilon_{e1}(\lambda) = u(-\lambda + \lambda_f)$$

$$\text{case 2:}\quad \varepsilon_{e2}(\lambda) = (\lambda_f - \lambda_o)^{-1} R(\lambda - \lambda_o) u(-\lambda + \lambda_f)$$

$$\text{case 3:}\quad \varepsilon_{e3}(\lambda) = (\lambda_f - \lambda_o)^{-1} R(-\lambda + \lambda_o) u(-\lambda + \lambda_f)$$

$$\text{case 4:}\quad \varepsilon_{e4}(\lambda) = u(\lambda - \lambda_i) u(-\lambda + \lambda_f)$$

where λ_o and λ_i signify transition wavelengths where nonzero spectrum values appear in ε_{e2}, ε_{e3}, or ε_{e4}, and λ_f indicates a transition wavelength where the spectrum values fall into zero. Figure 2a–d presents the effective emittance spectra ($M_{e,eff1}$, $M_{e,eff2}$, $M_{e,eff3}$, and $M_{e,eff4}$), together with the emittance spectra (M_{e1}, M_{e2}, M_{e3}, and M_{e4}) at 1250 °C for emissivities of ε_{e1}, ε_{e2}, ε_{e3}, and ε_{e4}, respectively. Gallium antimonide (GaSb; $\lambda_{bg} \approx$

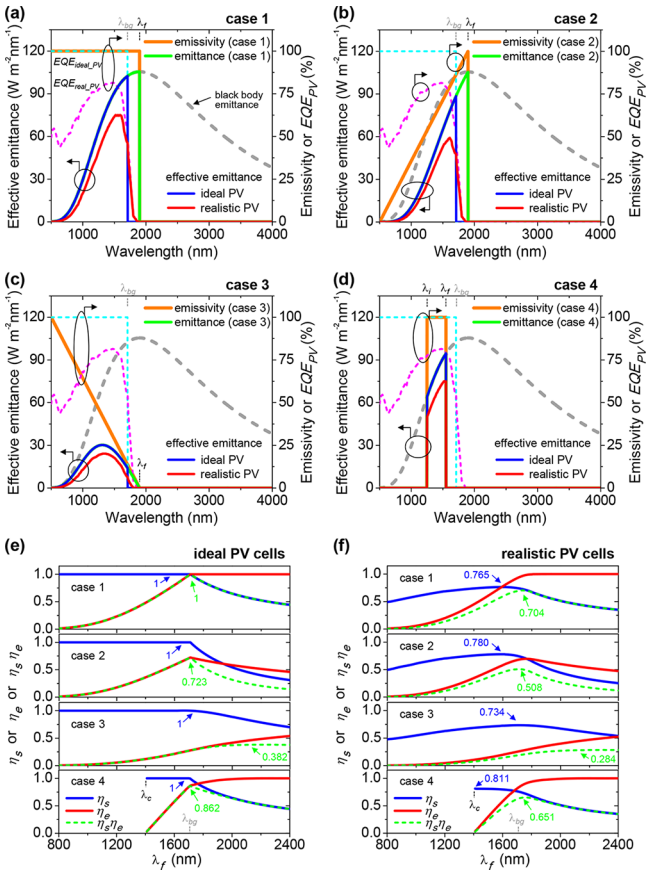

Figure 2. (a–d) Effective emittance spectra for the representative emissivities of (a) ε_{e1} (case 1), (b) ε_{e2} (case 2), (c) ε_{e3} (case 3), and (d) ε_{e4} (case 4) for the absorber types of ideal and realistic GaSb PV cells, respectively, under operation at 1250 °C. The emissivity and emittance spectra of each emitter case, as well as the EQE_{ideal_PV}, EQE_{real_PV}, and blackbody emittance spectra, are also displayed for comparison and clarity. (e, f) Calculated spectral cutoff efficiency (η_s), effective emittance efficiency (η_e), and $\eta_s\eta_e$ product values of the corresponding emissivities of ε_{e1}, ε_{e2}, ε_{e3}, and ε_{e4} as a function of the λ_f value for the absorber types of (e) ideal and (f) realistic GaSb PV cells. The λ_o values for ε_{e1}, ε_{e2}, and ε_{e3} are fixed to 500 nm, and the λ_i value for ε_{e4} is set to (2800 nm − λ_f).

DOI: 10.1021/acsphotonics.9b00560
ACS Photonics 2019, 6, 2260–2267

1708 nm) PV cells of the common TPV systems were employed as a radiation absorber, where their EQE_{PV} spectrum was assumed to be ideal ($EQE_{ideal\_PV}(\lambda) = 1$ for $\lambda < \lambda_{bg}$) or realistic ($EQE_{real\_PV}(\lambda)$ obtained from the commercialized cells[32]). When comparing the emittance spectra (M_{e1}, M_{e2}, and M_{e3}) of ε_{e1}, ε_{e2}, and ε_{e3} at fixed λ_o of 500 nm and λ_f of 1900 nm, it can be apparently found that the M_{e1} of a reverse unit step function ε_{e1} has the most preferable intensity values, as it follows the $M_{e,BB}$ until λ_f (Figure 2a). The M_{e2} calculated from a positively weighted reverse unit step function ε_{e2} shows reasonably high intensity values (Figure 2b), while the M_{e3} from a negatively weighted reverse unit step function ε_{e3} exhibits limited intensity values due to misalignment of ε_{e3} with $M_{e,BB}$ (Figure 2c). As ε_{e4} is a spectrum of the ε_{e1} after short-pass filtering at λ_i, band-pass-featured M_{e4} is observed accordingly (Figure 2d). The $M_{e,eff}$ at the ideal PV cells accurately follows the M_e until wavelengths below λ_{bg} and λ_f for all emissivities, whereas overall levels of the $M_{e,eff}$ at the realistic PV cells evidently decreases compared to the M_e. The relative decrease ratio of the $M_{e,eff}$ at the realistic PV cells is strongly dependent on correlation between the spectra of M_e and EQE_{real_PV}. The performances of emitters with these four emissivity spectra were compared with their characteristic factors. Figure 2e,f represents a variation of the η_s, η_e, and their product $\eta_s\eta_e$ values at 1250 °C, in accordance with an increase of λ_f, where λ_o values for ε_{e1}, ε_{e2}, and ε_{e3} were fixed to 500 nm and a λ_i value for ε_{e4} was determined by setting a center-wavelength ($\lambda_c = (\lambda_i + \lambda_f)/2$) of its passband to a peak wavelength (1400 nm) of the EQE_{real_PV} spectrum. In a case of the ideal PV cells, all emissivities hold a maximum η_s at λ_f values below λ_{bg} (Figure 2e), which means no superiority can be found among these emissivities if considering only η_s values. By contrast, when additionally taking into account η_e values, it can be recognized that the ε_{e1} is an exceptional emissivity that can seize a maximum η_e of 1 at λ_f values after λ_{bg}. Therefore, for TPV systems with the ideal PV cells, the reverse unit step function ε_{e1} with a value of λ_f same to λ_{bg} can be the optimum spectrum shape of emissivity. On the other hand, when the realistic PV cells are installed, a highest η_s value is observed at the emissivity ε_{e4}, with λ_f of around λ_c, as a consequence of minimized loss arising from the limited EQE_{real_PV} values. In terms of the η_e value, the emissivity ε_{e4} shows the superior performance as well, thereby retaining a reasonably high value of $\eta_s\eta_e$ product that is a crucial indicator under a condition of the large conduction or convection loss. Accordingly, from the result of a higher η_s value of the ε_{e4} than that of the ε_{e1}, an emissivity spectrum with a definite peak aligned with wavelengths of the EQE_{real_PV} peak is more suitable for achieving the high performance TPVs containing the realistic PV cells. It is noteworthy that there is no significant difference in η_e values between the cases of ideal and realistic PV cells, while substantial reduction in η_s values takes place by altering the absorber from ideal cells to realistic cells. At the different temperatures (e.g., 750, 1250, and 1500 °C), analogous conclusions can be made as shown in Figures S5–S7 of the Supporting Information.

With the established characteristic factors of emissivity spectra, studies for designing optimum Ni IO emitters passivated by a 30 nm thick MgO layer at the GaSb absorber system were implemented by using three-dimensional numerical finite-difference time-domain (FDTD) simulations over a manageable parameter of IO period, as shown in Figure 3. Here, the emissivity was calculated on the basis of the

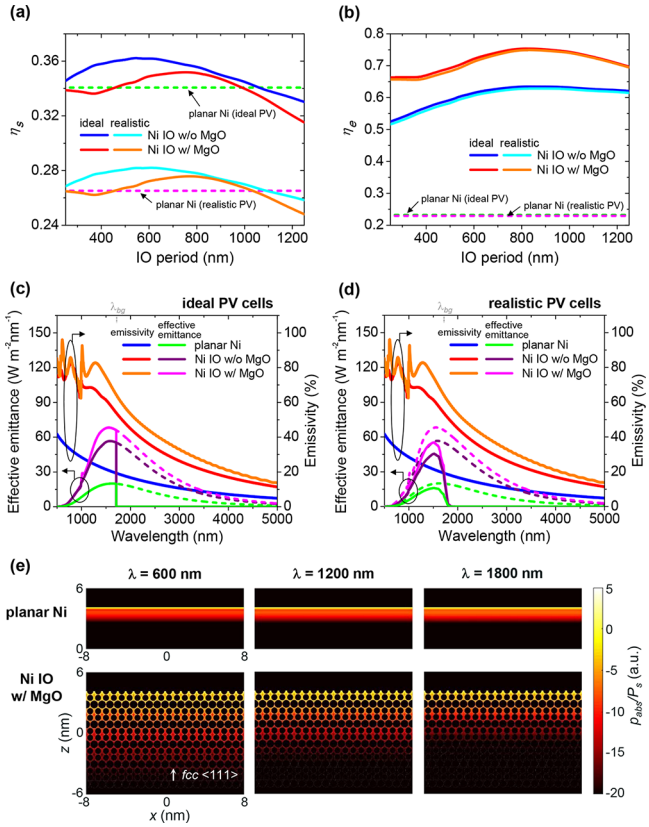

Figure 3. (a, b) Calculated (a) spectral cutoff efficiency (η_s) and (b) effective emittance efficiency (η_e) values of the Ni IO emitters with and without a 30 nm thick MgO passivation layer as a function of the IO period for the absorber types of ideal and realistic GaSb PV cells, respectively, at a working temperature of 1250 °C. Those of the planar Ni emitters are also depicted for comparison. (c, d) Calculated effective emittance and emissivity spectra for the planar Ni and optimal (period = 800 nm) Ni IO emitters with and without the MgO passivation for the absorbers of (c) ideal and (d) realistic GaSb PV cells. (e) Contour plots of the calculated absorbed power density (p_{abs}) normalized by source power (P_s) for the planar Ni (top) and MgO-passivated Ni IO (bottom) emitters at selected wavelengths of 600 (left), 1200 (middle), and 1800 nm (right), respectively.

Kirchhoff's law (i.e., emissivity = absorptivity), and its spectrum was postulated to be independent of the temperature. In the graph for calculated η_s values at 1250 °C in Figure 3a, it can be found that bare Ni IO (i.e., without MgO passivation) and MgO-passivated Ni IO gain the maximum η_s values at IO periods of ~600 and ~800 nm, regardless of PV cell configurations, respectively, where the maximum η_s values of both Ni IOs with and without MgO passivation are manifestly larger than those of planar Ni because of the spectral absorption property of Ni IO induced by the wavelength-selective plasmonic resonance. Meanwhile, it is a well-known fact that the plasmonic resonance of metallic nanostructures at a given pattern period becomes red-shifted and broad in wavelength if a higher-index passivation layer is introduced due to the increased effective refractive index of their surrounding media.[33−35] This statement implies that a pattern period of metallic nanostructures after applying a passivation layer has to be decreased to support the similar cutoff wavelength of absorptivity spectrum (due to the red-shifted resonance), and the cutoff performance tends to be inferior (because of the broadened resonance in wavelength).

DOI: 10.1021/acsphotonics.9b00560
ACS Photonics 2019, 6, 2260−2267

The theoretical anticipation regarding to poor cutoff performance at passivated nanostructures is undoubtedly valid in the present systems, as observed in the resultant η_s values of Ni IO with MgO smaller than those of bare Ni IO. However, the increased period of Ni IO for obtaining the maximum η_s value when introducing the MgO layer cannot be clearly elucidated only with the resonance shift behavior, because the effect of wavelength-dependent antireflection by a thin (30 nm) MgO layer is another element that affects the emissivity spectrum. This antireflection effect is absolutely conducive to reinforce the emittance, which results in boosting the η_e value (Figure 3b). Despite a considerable difference in the η_s values between absorber types of the ideal and realistic PV cells, the optimum period of MgO-passivated Ni IO emitters for the maximum performance can be determined as ~800 nm for both PV absorber cells due to their negligible difference in the spectrum shapes. The effective emittance and emissivity spectra of the optimum (i.e., period = 800 nm) Ni IO as well as bare Ni are displayed in Figure 3c and d for cases of the ideal and realistic PV absorber cells, respectively, in which relatively fast decay of the emissivity spectra, together with intensified effective emittance for Ni IOs can be confirmed. The enhanced absorption property of Ni IOs can be further clarified with the contour plots for absorbed power distribution of planar Ni and Ni IO with MgO at representative wavelengths of 600, 1200, and 1800 nm in Figure 3e, where a higher penetration depth can be found in the Ni IO case. It needs to be noted that the optimum period of Ni IOs is apt to move to the shorter level when the working temperature of emitters rises on account of the blue-shifted emittance peak, as depicted in Figures S8 and S9 of the Supporting Information.

As shown in Figure 4, experimental MgO-passivated (~30 nm) Ni IO samples with various periods (~250, ~500, ~750, and ~1250 nm) fabricated through processes described earlier were characterized by emissivity and effective emittance spectra that were derived from the measured absorptivity spectra. Although there is minor discrepancy between experimental samples and simulated models due to incomplete crystallinity of fabricated IO structures stemming from limited uniformity of sacrificial PS particles as well as their packing domain, the absolute levels and peak wavelengths of emissivity spectra measured with the Ni IO samples substantially correspond to those calculated with the modeling for all cases of IO periods (Figure 4a). As expected from the modeling, the emissivity levels of the Ni IO samples are considerably higher than those of the planar Ni sample, regardless of IO periods, where the near-optimum (period = ~750 nm) Ni IO sample particularly shows peak emissivity levels at wavelengths of ~1200 nm. With the effective emittance spectra of experimental samples at 1250 °C for the realistic GaSb PV absorber cells in Figure 4b, greatly improved radiation intensity in conjunction with meaningfully elevated cutoff behavior for the Ni IO samples can be explicitly identified. Additional information for the effective emittance spectra of the samples at other representative temperatures (750, 1000, and 1500 °C) are available in the Supporting Information (Figure S10).

The experimental investigation to substantiate the enhanced thermal stability of Ni IO emitters by introducing the MgO passivation is exhibited in Figure 5a,b, where SEM images and photographs were monitored for the near-optimum (period = ~750 nm) Ni IO emitter samples with and without a thin (~30 nm) MgO passivation layer after operation at 1100 °C

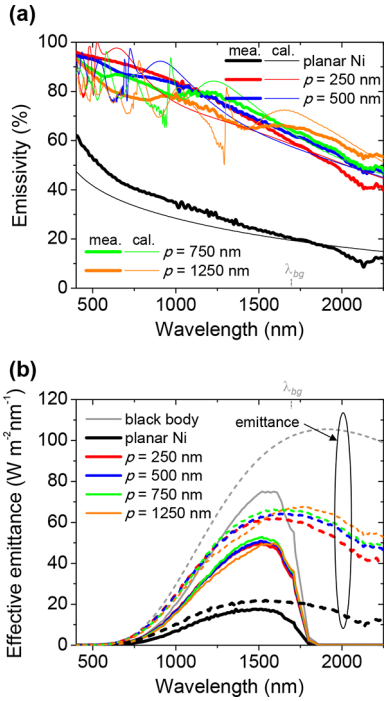

Figure 4. (a) Emissivity spectra obtained from the measured (thick lines) and calculated (thin lines) absorptivity spectra of the planar Ni and MgO-passivated Ni IO emitters with IO periods of 250, 500, 750, and 1250 nm. (b) Emittance and effective emittance spectra derived from the emissivity spectra measurement of (a) at a working temperature of 1250 °C. Those of the blackbody are additionally presented for comparison.

for an hour in an argon ambient condition. The IO structure of the unprotected Ni IO emitter utterly collapsed after operation (Figure 5a) by reason for the vigorous migration of Ni at this high temperature close to its melting point (~1450 °C), while the MgO-passivated Ni IO emitter was consistently sustained (Figure 5b), owing to the thermally stable ceramic material of MgO. Therefore, the characterized reflection color of operated Ni IO emitters is observed only at the sample protected with the MgO layer. Meanwhile, a photograph of working samples at 1100 °C in Figure 5c describes that even the visible photon radiation from the Ni IO emitter is apparently stronger than that from the planar Ni emitter, as expected in both simulation modeling and experimental measurement.

CONCLUSION

In summary, we reported wavelength-selective, nanostructured Ni IO emitters optimized through the proposed design scheme that employed the characterization factors of spectral cutoff efficiency and effective emittance efficiency to collectively consider the thermal loss as well as the radiation loss in the context of TPV system efficiency. The studies of conceivable emissivity spectra elucidated that the emissivity with band-pass-featured spectrum could be preferable than typical optimum emissivity with short-pass-featured spectrum unless the integrated PV cells were an ideal absorber. The numerically designed near-optimal Ni IO samples passivated with MgO showed the best emitter performance with a greatly increased value of the effective emittance efficiency and a reasonably improved value of the spectral cutoff efficiency owing to the plasmonic resonance at designated wavelengths. The enhanced thermal stability of Ni IOs by the MgO passivation was also

DOI: 10.1021/acsphotonics.9b00560
ACS Photonics 2019, 6, 2260−2267

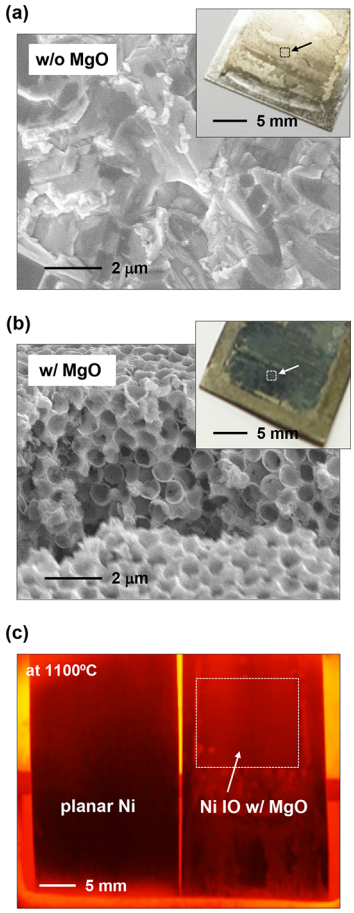

Figure 5. (a, b) Tilted-view SEM and photographic (inset) images of the near-optimal (period = ~750 nm) Ni IO emitters (a) without and (b) with the 30 nm thick MgO passivation after operation at 1100 °C for an hour in argon ambient condition. (c) Photographic image of the planar Ni (left) and MgO-passivated Ni IO (right) emitters working at 1100 °C.

identified from the operation test at a high temperature of ~1100 °C. The present studies cover not only emitter fabrications and characterizations, but also the design rule for high-performance emitters. We therefore anticipate these reported results can be readily applicable to further development of emitters in various classes of TPV systems.

METHODS

Fabrication of Three-Dimensional Ni IO Emitters. Fabrication of the Ni IO emitters began with the preparation of polystylene (PS) particles through the synthesis method desribed earlier.[28,29] Briefly, the styrene monomer (2 g) dissolved in the ethanol (25 mL) was mixed with polyvinylpyrrolidone (PVP, 25 mg) at 70 °C, followed by injecting the ammonium persulfate ($(NH_4)_2S_2O_8$, 96 mg) dissolved in water (3 mL) rapidly into this mixture. After reaction and washing with ethanol and water by centrifuging several times, the preparation of an aqueous PS particle solution (4 wt %) was completed, where a size of PS particles was determined by the reaction time. With the as-prepared PS particle solution, close-packed monolayer of PS particles was first formed on a polished Ni plate (thickness = ~100 μm) by the Langmuir–Blodgett method,[27] after which close-packed multilayers of PS particles were constructed on this seed monolayer by the slide-coating method.[28,29] Subsequently, the electrodeposition of Ni was conducted on the fabricated PS opal template through a system consisting of Ni (working electrode), Pt (counter electrode), Ag/AgCl (reference electrode), and $Ni(SO_3NH_2)_2/H_3BO_3$ (0.15 M/0.05 M) dissolved in water/ethanol (electrolyte). Following elimination of the PS opal template by toluene for 1 h manifested the Ni IO emitter. On this Ni IO emitter, a 30 nm thick MgO passivation layer was deposited by the thermal ALD system (Lucida D100) using $Mg(CpEt)_2$ and water at 70 °C.

Optical Characterization. The absorptivity spectra were obtained from measurement of the reflectance using the homemade optical system comprising visible (Maya 2000, Ocean Optics) and near-infrared (AvaSpec-NIR256–2.5-HSC-EVO, Avantes) spectrometers and fiber-optic integrating sphere, where a silver reflector was used as a 100% reflectance standard. The details of this setup can be found in Figure S11. To prepare the emitter samples working at a high temperature, they were heated in an argon-filled quartz tube furnace (LTF, Lenton) with a set temperature of 1100 °C (increase rate = 20 °C/min), where the operation time of samples was counted once the furnace temperature reached a set value.

Numerical Modeling of Ni IO Emitters. Optical characteristics of the Ni IO emitters were simulated with a commercial software on the basis on the FDTD method (FDTD Solutions, Lumerial). To design Ni IO structures, close-packed fcc background spheres with a refractive index of 1 were defined in a homogeneous medium of Ni, where a normally incident, continuous plane-wave with a broad Gaussian frequency spectrum (30–750 THz) was employed as a light source. In the case of MgO-passivated Ni IO structures, another class of spheres with MgO material properties was defined in advance of background spheres with a reduced size by a MgO thickness. Contour plots of absorbed power density (P_{abs}) normalized by the source power (P_s) at specific wavelengths were obtained from *E*-field profile calculations through the equation given by $p_{abs}(\vec{r},\lambda)/P_s = (\pi c/\lambda)|\vec{E}(\vec{r},\lambda)|^2 \, \mathrm{Im}[\varepsilon(\lambda)]/P_s$,[36,37] where c, $\vec{E}$, and ε are the speed of light, electric field, and permittivity of the medium, respectively. The refractive index of Ni was acquired from the literature,[38] while that of MgO was measured by the spectroscopic ellipsometer (M2000D, Woollam).

ASSOCIATED CONTENT

Supporting Information

The Supporting Information is available free of charge on the ACS Publications website at DOI: 10.1021/acsphotonics.9b00560.

Additional images of experimental samples, details of calculations, and measurement setup (Figures S1–S11) (PDF)

AUTHOR INFORMATION

Corresponding Authors

*E-mail: sungminlee@kookmin.ac.kr.
*E-mail: hyunjung@kookmin.ac.kr.

ORCID

Sung-Min Lee: 0000-0001-9446-9122

Notes

The authors declare no competing financial interest.

DOI: 10.1021/acsphotonics.9b00560
ACS Photonics 2019, 6, 2260–2267

■ ACKNOWLEDGMENTS

This work was supported by National Research Foundation of Korea (NRF) funded by the Ministry of Science, ICT under Grant Nos. NRF-2017M1A3A3A02016782, NRF-2013K1A4A3055679, NRF-2019R1C1C1008201, NRF-2017R1A2B2010552, and NRF-2015R1A5A7037615. The authors greatly acknowledge Prof. Mijung Lee and Prof. Sun-Kyung Kim for support of using fabrication and measurement facilities, respectively.

■ REFERENCES

(1) Coutts, T. J. A Review of Progress in Thermophotovoltaic Generation of Electricity. *Renewable Sustainable Energy Rev.* **1999**, *3*, 77−184.
(2) Bauer, T. *Thermophotovoltaics: Basic Principles and Critical Aspects of System Design*; Springer: Berlin, Heidelberg, 2011.
(3) Seyf, H. R.; Henry, A. Thermophotovoltaics: A Potential Pathway to High Efficiency Concentrated Solar Power. *Energy Environ. Sci.* **2016**, *9*, 2654−2665.
(4) Daneshvar, H.; Prinja, R.; Kherani, N. P. Thermophotovoltaics: Fundamentals, Challenges and Prospects. *Appl. Energy* **2015**, *159*, 560−575.
(5) Rinnerbauer, V.; Ndao, S.; Yeng, Y. X.; Chan, W. R.; Senkevich, J. J.; Joannopoulos, J. D.; Soljacic, M.; Celanovic, I. Recent Developments in High-Temperature Photonic Crystals for Energy Conversion. *Energy Environ. Sci.* **2012**, *5*, 8815−8823.
(6) Arpin, K. A.; Losego, M. D.; Cloud, A. N.; Ning, H. L.; Mallek, J.; Sergeant, N. P.; Zhu, L. X.; Yu, Z. F.; Kalanyan, B.; Parsons, G. N.; et al. Three-Dimensional Self-Assembled Photonic Crystals with High Temperature Stability for Thermal Emission Modification. *Nat. Commun.* **2013**, *4*, 2630.
(7) Dyachenko, P. N.; Molesky, S.; Petrov, A. Y.; Stormer, M.; Krekeler, T.; Lang, S.; Ritter, M.; Jacob, Z.; Eich, M. Controlling Thermal Emission with Refractory Epsilon-near-Zero Metamaterials via Topological Transitions. *Nat. Commun.* **2016**, *7*, 11809.
(8) Rinnerbauer, V.; Lenert, A.; Bierman, D. M.; Yeng, Y. X.; Chan, W. R.; Geil, R. D.; Senkevich, J. J.; Joannopoulos, J. D.; Wang, E. N.; Soljacic, M.; et al. Metallic Photonic Crystal Absorber-Emitter for Efficient Spectral Control in High-Temperature Solar Thermophotovoltaics. *Adv. Energy Mater.* **2014**, *4*, 1400334.
(9) Nam, Y.; Yeng, Y. X.; Lenert, A.; Bermel, P.; Celanovic, I.; Soljacic, M.; Wang, E. N. Solar Thermophotovoltaic Energy Conversion Systems with Two-Dimensional Tantalum Photonic Crystal Absorbers and Emitters. *Sol. Energy Mater. Sol. Cells* **2014**, *122*, 287−296.
(10) Lenert, A.; Bierman, D. M.; Nam, Y.; Chan, W. R.; Celanovic, I.; Soljacic, M.; Wang, E. N. A Nanophotonic Solar Thermophotovoltaic Device. *Nat. Nanotechnol.* **2014**, *9*, 126−130.
(11) Ganapati, V.; Xiao, T. P.; Yablonovitch, E. Ultra-Efficient Thermophotovoltaics Exploiting Spectral Filtering by the Photovoltaic Band-Edge. *arXiv:1611.03544v2 [physics.optics]* **2018**, na.
(12) Burger, T.; Fan, D. J.; Lee, K.; Forrest, S. R.; Lenert, A. Thin-Film Architectures with High Spectral Selectivity for Thermophotovoltaic Cells. *ACS Photonics* **2018**, *5*, 2748−2754.
(13) Durisch, W.; Bitnar, B. Novel Thin Film Thermophotovoltaic System. *Sol. Energy Mater. Sol. Cells* **2010**, *94*, 960−965.
(14) Ferguson, L. G.; Dogan, F. Spectrally Selective, Matched Emitters for Thermophotovoltaic Energy Conversion Processed by Tape Casting. *J. Mater. Sci.* **2001**, *36*, 137−146.
(15) Torsello, G.; Lomascolo, M.; Licciulli, A.; Diso, D.; Tundo, S.; Mazzer, M. The Origin of Highly Efficient Selective Emission in Rare-Earth Oxides for Thermophotovoltaic Applications. *Nat. Mater.* **2004**, *3*, 632−637.
(16) Bitnar, B.; Durisch, W.; Mayor, J. C.; Sigg, H.; Tschudi, H. R. Characterisation of Rare Earth Selective Emitters for Thermophotovoltaic Applications. *Sol. Energy Mater. Sol. Cells* **2002**, *73*, 221−234.
(17) Fleming, J. G.; Lin, S. Y.; El-Kady, I.; Biswas, R.; Ho, K. M. All-Metallic Three-Dimensional Photonic Crystals with a Large Infrared Bandgap. *Nature* **2002**, *417*, 52−55.
(18) Yeng, Y. X.; Ghebrebrhan, M.; Bermel, P.; Chan, W. R.; Joannopoulos, J. D.; Soljacic, M.; Celanovic, I. Enabling High-Temperature Nanophotonics for Energy Applications. *Proc. Natl. Acad. Sci. U. S. A.* **2012**, *109*, 2280−2285.
(19) Tian, Y. P.; Ghanekar, A.; Ricci, M.; Hyde, M.; Gregory, O.; Zheng, Y. A Review of Tunable Wavelength Selectivity of Metamaterials in Near-Field and Far-Field Radiative Thermal Transport. *Materials* **2018**, *11*, 862.
(20) Chou, J. B.; Yeng, Y. X.; Lenert, A.; Rinnerbauer, V.; Celanovic, I.; Soljacic, M.; Wang, E. N.; Kim, S. G. Design of Wide-Angle Selective Absorbers/Emitters with Dielectric Filled Metallic Photonic Crystals for Energy Applications. *Opt. Express* **2014**, *22*, A144−A154.
(21) Khorrami, Y.; Fathi, D. Broadband Thermophotovoltaic Emitter Using Magnetic Polaritons Based on Optimized One- and Two-Dimensional Multilayer Structures. *J. Opt. Soc. Am. B* **2019**, *36*, 662−666.
(22) Armstrong, E.; O'Dwyer, C. Artificial Opal Photonic Crystals and Inverse Opal Structures - Fundamentals and Applications from Optics to Energy Storage. *J. Mater. Chem. C* **2015**, *3*, 6109−6143.
(23) Yan, Q. F.; Nukala, P.; Chiang, Y. M.; Wong, C. C. Three-Dimensional Metallic Opals Fabricated by Double Templating. *Thin Solid Films* **2009**, *517*, 5166−5171.
(24) Hossain, M. M.; Gu, M. Fabrication Methods of 3d Periodic Metallic Nano/Microstructures for Photonics Applications. *Laser Photon. Rev.* **2014**, *8*, 233−249.
(25) Jones, W. M.; Zhang, R. Y.; Murty, E.; Zhu, X. T.; Yao, Y. F.; Manohara, H.; Braun, P. V.; Montemayor, L. C. Field Emitters Using Inverse Opal Structures. *Adv. Funct. Mater.* **2019**, *29*, 1808571.
(26) Bratsch, S. G.; Lagowski, J. J. Predicted Stabilities of Monatomic Anions in Water and Liquid-Ammonia at 298.15 K. *Polyhedron* **1986**, *5*, 1763−1770.
(27) Oh, J. R.; Moon, J. H.; Yoon, S.; Park, C. R.; Do, Y. R. Fabrication of Wafer-Scale Polystyrene Photonic Crystal Multilayers via the Layer-by-Layer Scooping Transfer Technique. *J. Mater. Chem.* **2011**, *21*, 14167−14172.
(28) Gil, S. C.; Seo, Y. G.; Kim, S.; Shin, J.; Lee, W. High-Speed Fabrication of 3-Dimensional Colloidal Photonic Crystal Films by Slide Coating of Polymer Microspheres with Continuous Feeding of Colloidal Suspension. *Thin Solid Films* **2010**, *518*, 5731−5736.
(29) Kim, S.; Koh, Y. G.; Lee, H.; Lee, W. Flexible Polymer Opal Films Prepared by Slide Coating from Alcoholic Media. *Macromol. Res.* **2017**, *25*, 415−419.
(30) Sumida, T.; Wada, Y.; Kitamura, T.; Yanagida, S. Construction of Stacked Opaline Films and Electrochemical Deposition of Ordered Macroporous Nickel. *Langmuir* **2002**, *18*, 3886−3894.
(31) Kim, E.; Han, Y.; Kim, W.; Choi, K. C.; Im, H. G.; Bae, B. S. Thin Film Encapsulation for Organic Light Emitting Diodes Using a Multi-Barrier Composed of Mgo Prepared by Atomic Layer Deposition and Hybrid Materials. *Org. Electron.* **2013**, *14*, 1737−1743.
(32) JX Crystals Sale Items. http://jxcrystals.com/GaSb/4sale5.pdf (accessed 25 June).
(33) Lee, S. M.; Chae, J. S.; Kim, D. Y.; Choi, K. C. Plasmonic Nanomeshes as Large-Area, Low-Resistive Transparent Electrodes and Their Application to ITO-Free Organic Light-Emitting Diodes. *Org. Electron.* **2014**, *15*, 3354−3361.
(34) Lee, S. M.; Cho, Y.; Kim, D. Y.; Chae, J. S.; Choi, K. C. Enhanced Light Extraction from Mechanically Flexible, Nanostructured Organic Light-Emitting Diodes with Plasmonic Nanomesh Electrodes. *Adv. Opt. Mater.* **2015**, *3*, 1240−1247.
(35) Do, Y. S.; Park, J. H.; Hwang, B. Y.; Lee, S. M.; Ju, B. K.; Choi, K. C. Plasmonic Color Filter and Its Fabrication for Large-Area Applications. *Adv. Opt. Mater.* **2013**, *1*, 133−138.
(36) Lee, S. M.; Biswas, R.; Li, W. G.; Kang, D.; Chan, L.; Yoon, J. Printable Nanostructured Silicon Solar Cells for High-Performance, Large-Area Flexible Photovoltaics. *ACS Nano* **2014**, *8*, 10507−10516.

DOI: 10.1021/acsphotonics.9b00560
ACS Photonics 2019, 6, 2260−2267

(37) Lee, S. M.; Kwong, A.; Jung, D.; Faucher, J.; Biswas, R.; Shen, L.; Kang, D.; Lee, M. L.; Yoon, J. High Performance Ultrathin GaAs Solar Cells Enabled with Heterogeneously Integrated Dielectric Periodic Nanostructures. *ACS Nano* **2015**, *9*, 10356−10365.
(38) Palik, E. D. *Handbook of Optical Constants of Solids*; Academic Press, 1998; Vol. 3.

DOI: 10.1021/acsphotonics.9b00560
ACS Photonics 2019, 6, 2260−2267